ADVANCED FUNCTIONAL MATERIALS
www.afm-journal.de

Iron-Cobalt Co-Doped Nickel Sulfides: A Robust Electrocatalyst for High-Current-Density Seawater Splitting

You-li Sun, You-yi Sun, Yuxuan Zhang, Takeshi Yanagida, Johnny C. Ho,* and SenPo Yip**

Nickel–iron-based sulfides have recently attracted considerable attention as promising candidates for water oxidation. However, the high concentration of chloride ions (Cl^-) in seawater poses a major challenge, as they readily corrode active sites and significantly compromise long-term durability. Most nickel–iron-based sulfides suffer from poor stability under these conditions, particularly at high current densities, which greatly hinders their practical application in large-scale seawater electrolysis. In this study, an innovative iron and cobalt co-doped nickel sulfide (NiFeCoS) electrode is introduced, produced via a simple fabrication method, which effectively protects the active sites from Cl^- attack during alkaline seawater oxidation, even under high current densities. The NiFeCoS catalyst exhibits remarkable stability, maintaining stable performance for over 148 h at a current density of 1 A cm^{-2} in alkaline seawater electrolytes. In an alkaline electrolyte, it achieves low overpotentials of 261, 312, and 342 mV to reach current densities of 100, 500, and 1000 mA cm^{-2}. This research presents a novel approach for constructing NiFeCoS electrodes through a straightforward two-step synthesis process, offering a promising and efficient strategy for large-scale hydrogen production via seawater electrolysis.

1. Introduction

The renewable energy sector is pivotal for the sustainable advancement of human society. Hydrogen, with its impressive energy density and environmentally benign byproducts, has attracted substantial interest worldwide.[1–4] However, traditional hydrogen production methods heavily rely on fossil fuels, contradicting the fundamental goal of fostering clean and pollution-free hydrogen energy. Electrochemical water splitting, powered by renewable sources, is recognized as a viable solution for generating clean and sustainable hydrogen fuel on a large scale, addressing both the global energy crisis and environmental concerns.[5–7]

Freshwater, constituting a mere fraction of the Earth's total water reserves, is unevenly distributed and limited in availability. Most current water electrolysis processes depend on freshwater as the primary electrolyte, raising concerns about potential resource strain as hydrogen demand escalates.[8–10] Conversely, seawater, which comprises ≈96.5% of the planet's water resources, offers a more abundant and evenly distributed alternative. Direct seawater electrolysis emerges as an innovative industrial and large-scale hydrogen production strategy.[9–12]

Despite its advantages, electrocatalytic seawater splitting faces several challenges. The competition between the chlorine evolution reaction (ClER) and the oxygen evolution reaction (OER) in seawater electrolysis diminishes system efficiency due to the high concentration of chloride ions (≈0.5 M) in seawater.[11–14] Effective electrocatalytic seawater splitting necessitates anodes with high oxygen evolution selectivity, particularly limiting the OER overpotential to within 490 mV to prevent hypochlorite formation.[15–18] Furthermore, the formation of insoluble precipitates like $Mg(OH)_2$ and $Ca(OH)_2$ on the electrode surface during electrolysis reduces the active area for electrocatalysis, further impeding catalyst efficiency.[19]

The competitive interaction between ClER and OER in seawater electrolysis was first identified by Bennett, prompting numerous researchers to explore practical strategies for preparing electrocatalysts that exhibit high activity and stability for hydrogen evolution reactions (HER) and the OER.[20] Among various electrocatalyst types, transition metal sulfides (TMSs) have gained significant attention as promising candidates due to their affordability, abundance, unique band structure, and excellent

Y.-li Sun
Interdisciplinary Graduate School of Engineering Sciences
Kyushu University
Kasuga, Fukuoka 816-8580, Japan
Y.-yi Sun
Environmental Science and New Energy Technology Research Center
Tsinghua Shenzhen International Graduate School
Tsinghua University
Shenzhen 518055, P. R. China
Y. Zhang, J. C. Ho
Department of Materials Science and Engineering
City University of Hong Kong
Hong Kong, SAR 999077, P. R. China
E-mail: johnnyho@cityu.edu.hk
T. Yanagida
Department of Applied Chemistry
Graduate School of Engineering
The University of Tokyo
Tokyo 113-8656, Japan
E-mail: yanagida@g.ecc.u-tokyo.ac.jp
J. C. Ho, S. Yip
Institute for Materials Chemistry and Engineering
Kyushu University
Kasuga-koen 6-1, Kasuga, Fukuoka 816-8580, Japan
E-mail: yip.sen.po.472@m.kyushu-u.ac.jp

DOI: 10.1002/adfm.202517978

electrocatalytic properties.[21–25] Compared to transition metal oxides, TMS-based materials generally offer superior electrical conductivity, attributed to their smaller bandgap and semiconducting properties. 2D TMSs, in particular, boast a large specific surface area, remarkable stability, and numerous exposed active sites, resulting in exceptional catalytic performance for both the HER and the OER.[23,26]

Moreover, unlike metal carbides and nitrides, which typically require complex high-temperature synthesis, and metal phosphides, which often release toxic gases during production, TMS materials can be synthesized under relatively mild conditions.[27,28] Extensive research on various TMSs (such as MoS_2, Ni_3S_2, and FeS) has demonstrated their significant potential as catalysts for the OER and the HER. Through approaches like surface engineering, phase structure control, and composition regulation, the activity of some TMS-based electrocatalysts has approached that of noble metal catalysts.[29,30] Nevertheless, challenges remain for the practical application of TMSs, including their instability at oxidation potentials and inevitable conversion into corresponding oxides or oxysulfides.[31] Moreover, studies validating their stability under high current density in saline environments are scarce.

In this study, we introduce a novel corrosion-resistant NiFeCoS with a nanosheet morphology, synthesized on nickel foam (NF) through a straightforward room-temperature process followed by solvothermal treatment. The optimized catalyst requires 362 and 392 mV to achieve a current density of 1 A cm^{-2} in alkaline saline and seawater electrolytes, respectively. It demonstrates exceptional stability, with minimal degradation for over 100 h at 0.5 A cm^{-2} in alkaline seawater electrolytes. The incorporation of Co species effectively tunes the local electronic structure of Fe-doped Ni_3S_2 (NiFeS), significantly enhancing its resistance to chloride-induced corrosion. Density functional theory (DFT) results reveal that Co species synergistically enhance the ionic selectivity of the catalysts. This study offers a promising strategy for designing highly efficient and stable TMS-based electrocatalysts for industrial-scale alkaline seawater electrolysis.

2. Results and Discussion

2.1. Synthesis and Characterization of NiFeS and NiFeCoS Nanosheets

NF was selected as the substrate due to its high electrical conductivity, porous structure, and excellent resistance to sulfur-containing solutions. **Figure 1a** presents a schematic illustration of the two-step synthesis method used to synthesize NiFeS and NiFeCoS nanosheets on NF. The process involves first synthesizing NiFe(Co) layered double hydroxide (NiFe(Co) LDH) nanosheet arrays on NF at room temperature, followed by vulcanization through a solvothermal process. The detailed procedure was presented in the Experimental Section (Supporting Information). As shown in Figure S2 (Supporting Information), the photographic image shows changes in the surface color of NF in each stage. The catalyst morphology was analyzed using scanning electron microscopy (SEM) and transmission electron microscopy (TEM). The SEM images of NiFeCoS and NiFeS in Figures 1b and S3b (Supporting Information) reveal that the NF surface is covered with a layer of thin nanosheets arranged in neat and uniform arrays. These nanosheet arrays provide a large surface area and abundant active sites for water electrolysis, enhance electrolyte dispersion, and facilitate bubble release.[32] Additionally, the NiFeS nanosheets appear relatively thin (Figure S3b, Supporting Information). With Co doping, the thickness of the nanosheets increases (Figure 1b), indicating that Co influences the morphology of the nanosheet structure. Further structural characterization was conducted using TEM imaging of the NiFeS and NiFeCoS. Figure 1c,f show that NiFeS and NiFeCoS maintain a stacked nanosheet structure. The standard lattice spacings of the (003) and (202) crystal planes of Ni_3S_2 (PDF#44-1418) are 0.238 and 0.204 nm, respectively. Due to the Fe doping, the lattice of Ni_3S_2 becomes smaller after the formation of NiFeS.[33] High-resolution TEM (HR-TEM) imaging revealed lattice spacings of 0.235 and 0.203 nm, corresponding to the (003) and (202) crystal planes of Ni_3S_2 (Figure 1d). With the co-introduction of Co and Fe atoms, the HR-TEM imaging revealed further reduced lattice spacings of 0.232 and 0.200 nm, corresponding to the (003) and (202) crystal planes of Ni_3S_2 (Figure 1g).[33,34] The well-resolved lattice fringes of the samples were presented in Figures S4 and S5 (Supporting Information). The lattice distortion was further confirmed by selected area electron diffraction (SAED) patterns (Figure 1e,h). Figure 1e displays typical diffraction patterns indexed to the (003), (022), (133), and (040) planes of NiFeS, while Figure 1h shows diffraction rings indexed to the (003), (022), (133), and (040) planes of NiFeCoS. These patterns align well with the obtained X-ray diffraction (XRD) patterns (discussed later). High-angle annular dark-field scanning transmission electron microscopy (HAADF-STEM) images, combined with the energy dispersive spectroscopy (EDS) analysis mapping, revealed a homogeneous distribution of Fe, Ni, Co, and S elements (Figures 1i; S3c, Supporting Information). EDS results further indicate that the atomic ratio of Ni, Fe, and Co in the prepared NiFeS and NiFeCoS nanosheet arrays is 21:1 and 36:2:1, respectively (Table S1, Supporting Information). The ICP-OES results quantitatively display the elemental ratios of the two sulfides (Table S2, Supporting Information). The ratios of the Fe/Co are consistent with the TEM-EDX results.

The crystal structure of the samples was further analyzed using XRD. As shown in Figure S6 (Supporting Information), the diffraction peaks of the as-synthesized NiFe LDH closely match the standard XRD patterns of NiFe LDH (PDF#49–0188). Upon the introduction of Co atoms, the intensity of the diffraction peaks significantly decreases, indicating the successful formation of NiFeCo LDH nanosheets on the NF surface and a reduction in the crystallinity of the NiFeCo LDH nanosheets.[33] Based on the standard diffraction pattern of Ni_3S_2 (PDF#44-1418), the characteristic peaks at 31.10°, 37.78°, 49.73°, 50.12°, and 55.16° correspond to the (110), (003), (113), (211), and (122) crystal planes of Ni_3S_2, respectively. For the as-synthesized NiFeS, the diffraction peaks at 32.17°, 38.20°, 51.21°, 51.28°, and 56.38° correspond to the (110), (003), (113), (211), and (122) crystal planes. Introducing Fe decreases the intensity of diffraction peaks, suggesting increased lattice disorder.[33,35] Furthermore, with the introduction of Co, the diffraction peaks of the NiFeCoS at 32.37°, 51.37°, 51.46°, and 56.57° correspond to the (110), (113), (211), and (122) crystal planes. A significant rightward shift in the diffraction peaks is observed with the introduction of Co, attributed to the smaller atomic radius of Co^{2+} than Ni^{2+}, which

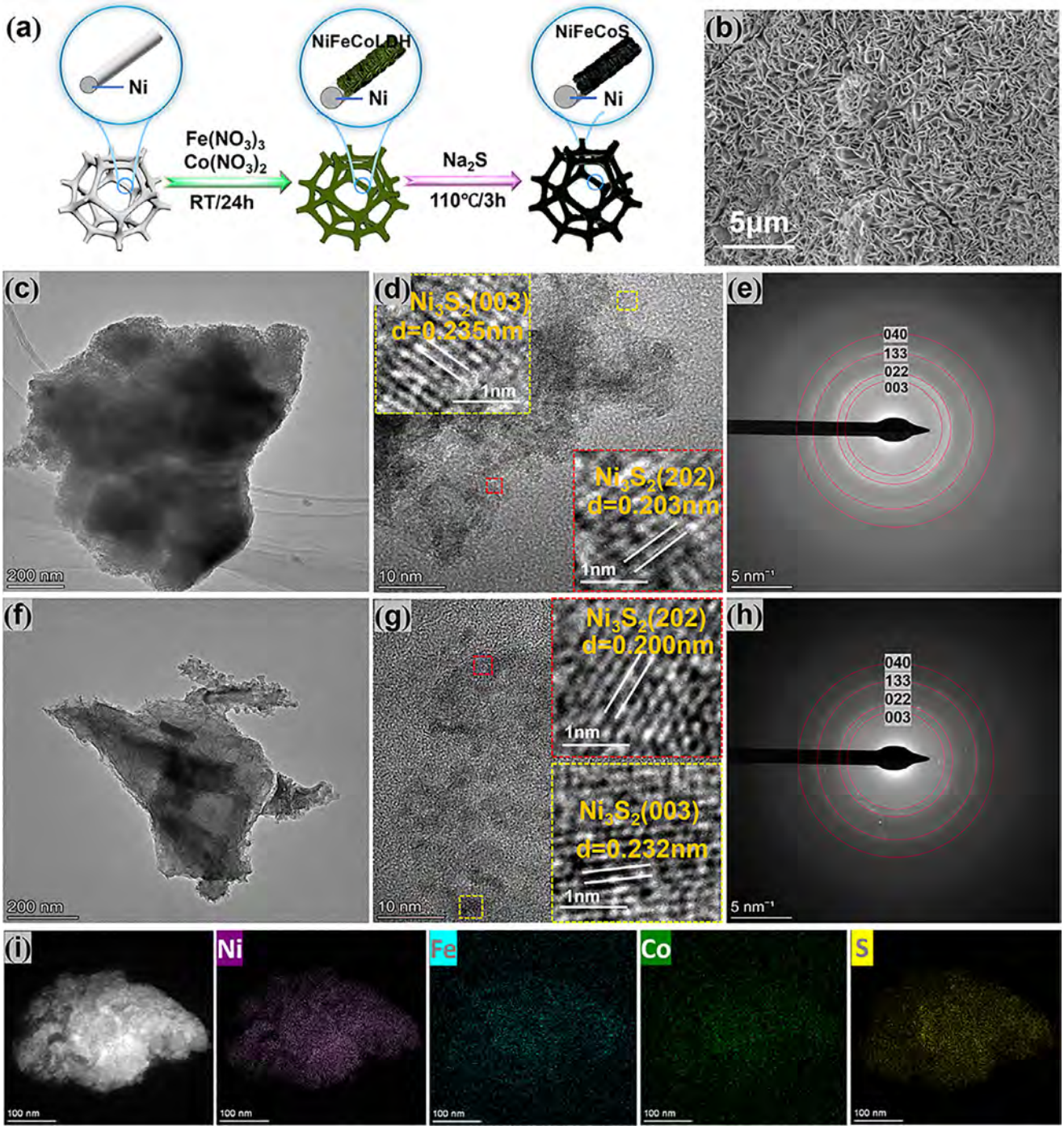

Figure 1. Microstructures of NiFeS and NiFeCoS. a) Schematic illustration of the synthesis process of NiFeCoS. b) FE-SEM image of NiFeCoS. c,f) TEM images of NiFeS and NiFeCoS. d,g) HR-TEM images of NiFeS and NiFeCoS (insets: lattice fringes corresponding to the (003) and (202) facets). e,h) SAED patterns of NiFeS and NiFeCoS (the scale bars in e and f are 5 nm^{-1}). i) HAADF-STEM image and corresponding element mappings of NiFeCoS.

induces a change in the diffraction peaks.[33–35] These XRD results align with the TEM observation, confirming that the incorporation of Co induces lattice distortion.

X-ray photoelectron spectroscopy (XPS) was performed to analyze the surface chemical composition and valence states. In the high-resolution spectrum of Ni 2p (Figure 2b), two characteristic peaks at 855.2 and 873.1 eV correspond to Ni $2p_{3/2}$ and Ni $2p_{1/2}$ of the NiFeS sample.[36] Upon Co incorporation, these peaks shift slightly to 855.9 and 873.4 eV, indicating a positive shift. The high-resolution XPS spectrum of Fe 2p (Figure 2c) shows the two peaks at 725.5 and 711.7 eV in NiFeS, corresponding to Fe $2p_{1/2}$ and Fe $2p_{3/2}$, respectively.[37] With the introduction of Co, the Fe

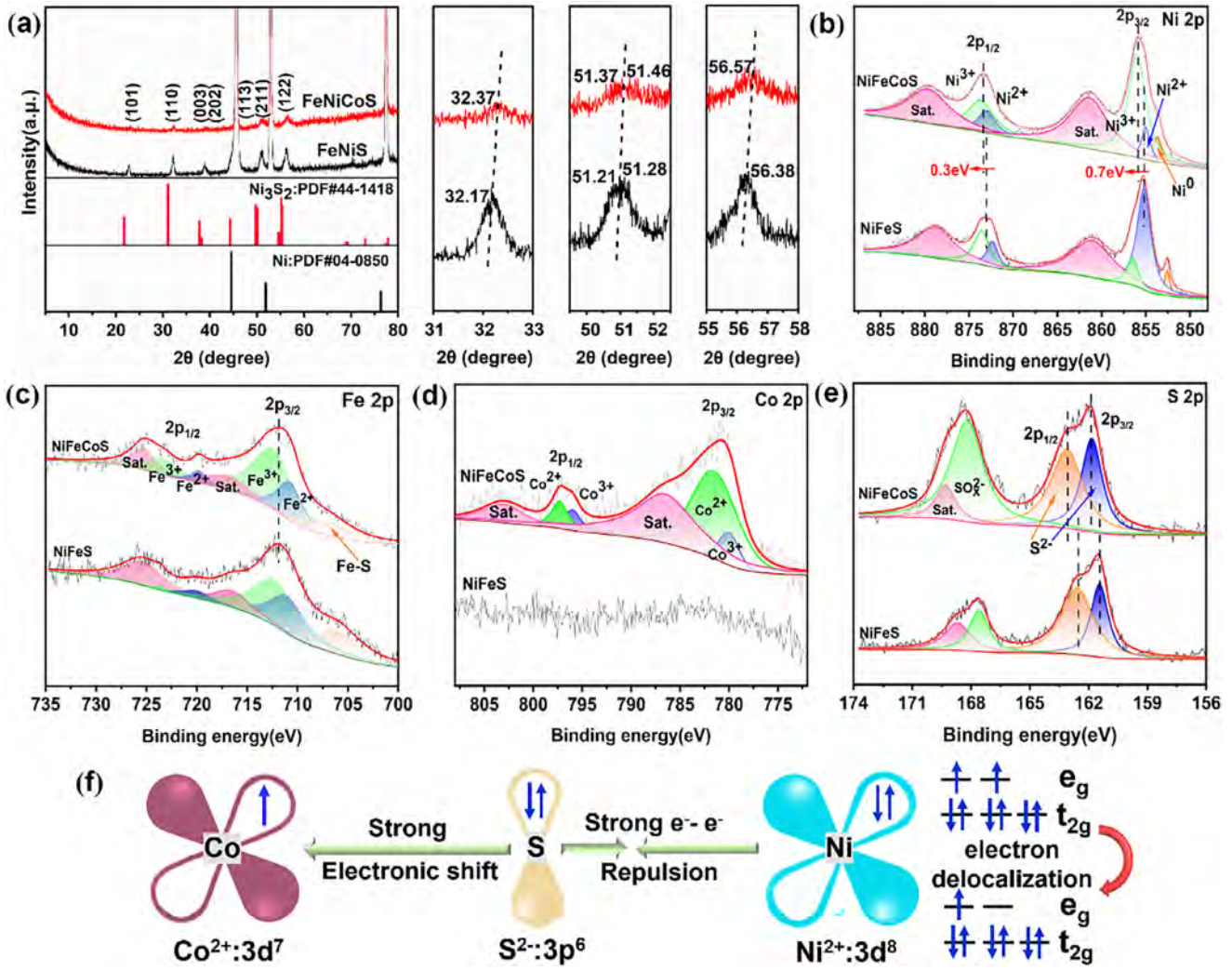

Figure 2. Crystal structure and surface chemical states characterization. a) XRD patterns of NiFeS and NiFeCoS. High-resolution XPS spectra of b) Ni 2p, c) Fe 2p, d) Co 2p, and e) S 2p of NiFeS and NiFeCoS. f) Schematic illustration of the electronic interactions in NiFeCoS catalyst and the orbital splitting of Ni 3d.

$2p_{1/2}$ peak exhibits a slightly negative shift of 0.5 eV. Notably, the peak area ratios of Ni^{2+}/Ni^{3+} and Fe^{2+}/Fe^{3+} for the NiFeS electrocatalyst are larger than those of the NiFeCoS electrocatalyst (Table S6, Supporting Information), indicating that Ni^{2+}/Fe^{2+} are transformed into Ni^{3+}/Fe^{3+} species with the Co doping.[38] Co doping also induces a significant shift in the S spectrum, suggesting that Co modifies the electronic structure of Ni, Fe, and S.[39] Ni 2p and Fe 2p peaks shift toward higher binding energy, indicating the increased valence states of both Ni and Fe species for NiFeCoS. The combined XRD and XPS results confirm the formation of Co—S—Ni bonds in the NiFeCoS catalyst. A structural illustration of the Co—S—Ni unit is provided in Figure 2f, highlighting the electronic interactions among Ni, S, and Co atoms. Here, the S atoms in the Co—S—Ni bond create an efficient electron transfer channel from Ni to Co, driven by their complementary orbital occupancy and diverse valence states. Specifically, Ni^{2+} species ($t_2g^6eg^2$), with fully occupied and π-symmetric (t_2g) orbitals, interact with the S atom due to strong electron–electron repulsion between Ni and Co. In contrast, the electron-deficient Co^{3+}/Co^{2+} species possess partially filled t_2g d-orbitals, enabling strong orbital coupling with S. This asymmetry facilitates spontaneous electron transfer from Ni to Co via S, inducing an orbital electron equilibrium that optimizes the electronic structure. As a result, the adsorption of OER intermediates is improved, enhancing ion selectivity and overall catalytic performance.

2.2. OER Performance of NiFeS and NiFeCoS Nanosheets in Alkaline Saline Medium at High Current Density

The hydrophilicity of the electrode plays a critical role in water splitting. Therefore, the water contact angle of NiFeS and NiFeCoS was studied and shown in Figure S8 (Supporting Information), demonstrating the good hydrophilicity of NiFeS and NiFeCoS. After that, the electrocatalytic performance of the NiFeS and NiFeCoS catalysts for the OER was evaluated in 1.0 M KOH

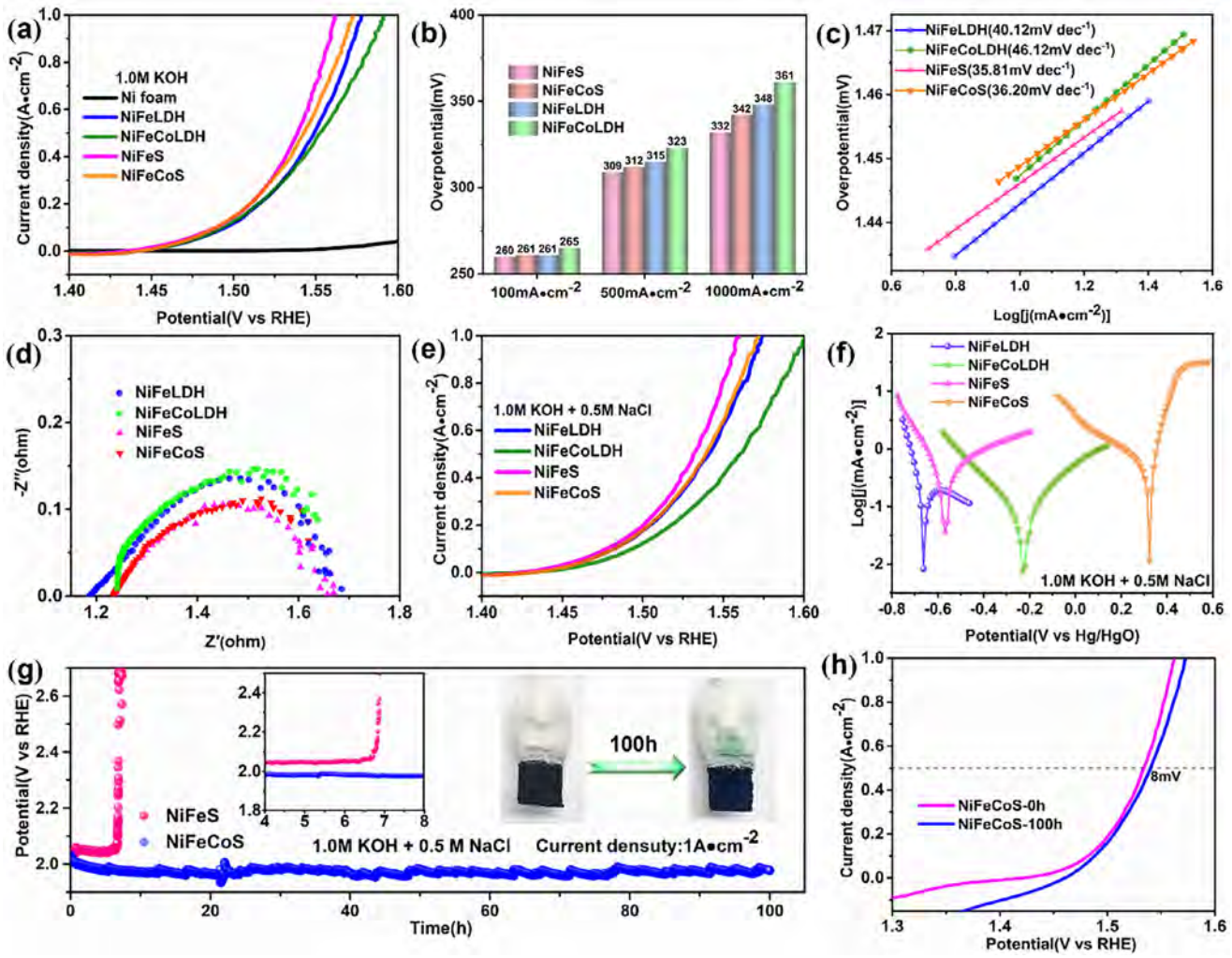

Figure 3. Electrocatalytic properties were characterized in an alkaline electrolyte. a–d) LSV curves, overpotentials, Tafel plots, and EIS curves of NiFeS, NiFeCoS, NiFe LDH, and NiFeCo LDH electrodes in 1.0 M KOH. e) LSV curves of NiFeS, NiFeCoS, NiFe LDH, and NiFeCo LDH electrode in alkaline saline electrolyte. f) Polarization curves for NiFeS, NiFeCoS, NiFe LDH, and NiFeCo LDH electrode. g) Chronopotentiometry test of NiFeS and NiFeCoS electrode at 1 A cm^{-2} without ohmic compensation. h) LSV curves of NiFeCoS electrode before and after 100 h of operation.

solution, leveraging their nano-porous structures. The iR-corrected OER polarization curves were measured using a three-electrode system, with a Hg/HgO electrode as the reference electrode, a graphite rod as the counter electrode, and the fabricated electrocatalyst on NF as the working electrode. Linear sweep voltammetry (LSV) curves of different electrocatalysts (**Figure 3a**) were measured with a scan rate of 5 mV s^{-1} at room temperature. Among the tested samples, the NiFeS and NiFeCoS exhibit the best OER activities, achieving overpotentials of 260 and 261 mV at a current density of 100 mA cm^{-2}, respectively. This performance surpasses that of NiFe LDH and NiFeCo LDH. The NiFeS showed superior OER performance, requiring ultralow overpotentials of 260, 309, and 332 mV to reach current densities of 100, 500, and 1000 mA cm^{-2}, respectively. These values are slightly smaller than NiFeCoS (261, 312, and 342 mV), and significantly smaller than those of NiFe LDH (261, 315, and 348 mV), and NiFeCo LDH (265, 323, and 361 mV) under the same current densities (Figure 3b). The nickel component is known to serve as an active site in the OER process.[40] With the introduction of Co, some Ni sites are replaced (Tables S1 and S2, Supporting Information), potentially reducing the number of active sites. This accounts for the slightly higher overpotential of NiFeCoS compared to NiFeS. Tafel plots were derived from the corresponding polarization curves to assess the OER reaction kinetics and catalytic performance. As shown in Figure 3c, NiFeS exhibited the smallest Tafel slope (35.81 mV dec^{-1}), followed by NiFeCoS (36.20 mV dec^{-1}), NiFe LDH (40.12 mV dec^{-1}), and NiFeCo LDH (46.12 mV dec^{-1}). This indicates faster reaction kinetics for NiFeS and NiFeCoS, attributed to their enhanced adsorption and desorption of oxygenated intermediates.[29] Electrochemical impedance spectroscopy (EIS) was employed to evaluate the charge transfer behavior of the electrodes. The Nyquist plots are shown in Figure 3d. The charge transfer resistance of NiFeS is determined to be ≈0.48 Ω, slightly smaller than that of NiFeCoS (0.51 Ω), indicating more efficient charge transfer for NiFeS.

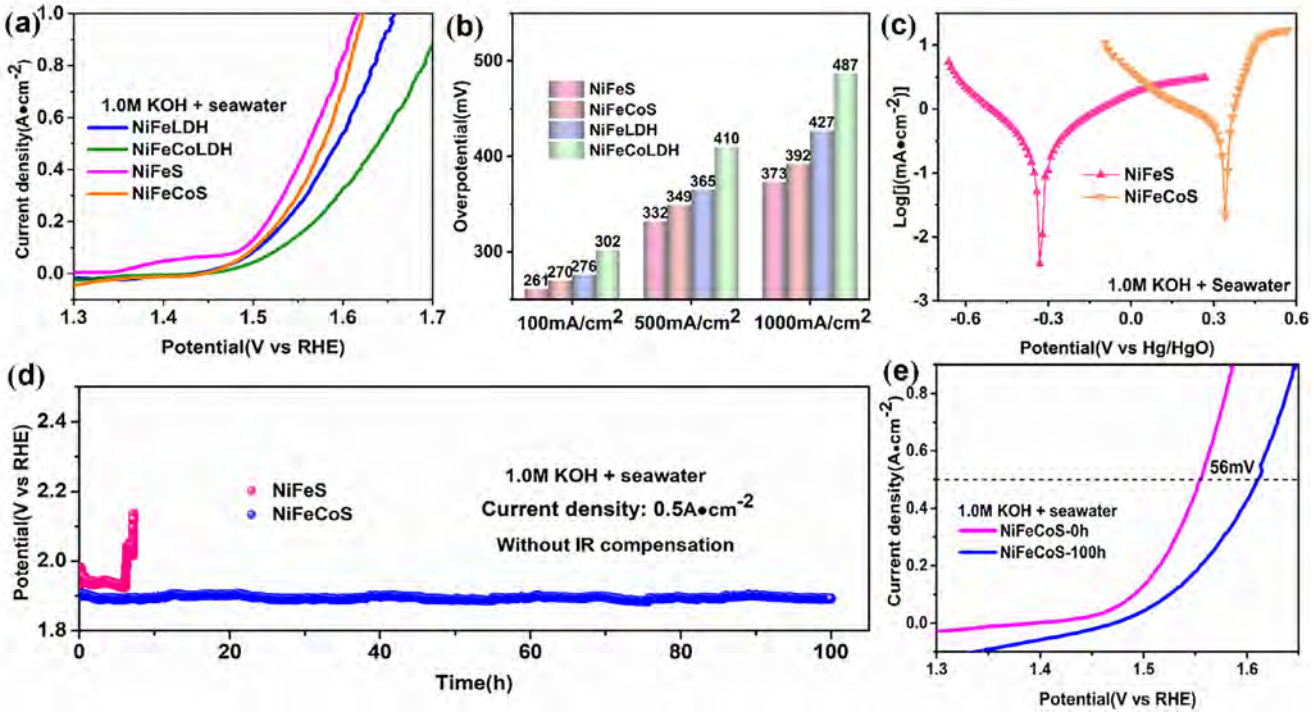

Figure 4. Electrocatalytic properties characterized in an alkaline seawater electrolyte. a,b) LSV curves and overpotentials of NiFeS, NiFeCoS, NiFe LDH, and NiFeCo LDH electrodes. c) Polarization curves for NiFeS and NiFeCoS. d) Chronopotentiometry test of NiFeS and NiFeCoS electrode at 0.5 A cm^{-2} without ohmic compensation. e) LSV curves of NiFeCoS electrode before and after 100 h of operation under 0.5 A cm^{-2}.

Building on the outstanding performance of NiFeS and NiFeCoS in alkaline water, OER measurements were extended to alkaline simulated seawater (1.0 M KOH + 0.5 M NaCl) to evaluate the robustness in saline environments. As shown in Figure 3e, the NiFeS showed ultralow overpotentials of 250, 300, and 330 mV in alkaline saline solution at current densities of 100, 500, and 1000 mA cm^{-2}, respectively. NiFeCoS also demonstrates remarkable OER activity under the same conditions, achieving overpotentials of 261, 327, and 362 mV at the same current densities. To further investigate corrosion resistance in the alkaline saline environment, the corrosion behaviors of the related catalysts were assessed in the same electrolyte (1.0 M KOH + 0.5 M NaCl). The corrosion voltage follows the order: NiFeCoS (0.323 V vs Hg/HgO) > NiFeCo LDH (−0.288 V vs Hg/HgO) > NiFeS (−0.564 V vs Hg/HgO) > NiFe LDH (−0.661 V vs Hg/HgO), as shown in Figure 3e and Table S7 (Supporting Information). The results confirm that Co doping significantly enhances the corrosion resistance of NiFeS in saline water electrolysis. Moreover, NiFeCoS exhibits excellent stability in alkaline saline environments (Figure 3f), demonstrating minimal performance degradation after 100 h of operation at a current density of 1 A cm^{-2} (Figure 3g). NiFeS can only sustain operation for less than 7 h under the same conditions. After 100 h of operation, the appearance of the material remains intact, as shown in the Figure 3g insert, and the poststability-test LSV curve (Figure 3h) overlaps with the original curve, showing only an 8 mV increase in overpotential at a commercialized current density of 0.5 A cm^{-2}. This highlights the superior resistance to chloride-induced corrosion. To further examine its Cl^- corrosion resistance, a comparative electrolytic lifespan test was conducted for NiFeS and NiFeCoS in 1.0 M KOH + 1.0 M NaCl, which represents a higher chloride concentration than in our prior experiments, at a current density of 1 A cm^{-2}, as shown in Figure S11 (Supporting Information). NiFeCoS demonstrates a stable operation for over 20 h, whereas NiFeS exhibits significant fluctuations, indicating minimal performance degradation of NiFeCoS. The experimental results confirm the excellent OER selectivity and corrosion resistance of NiFeCoS in saline water oxidation.

2.3. OER Performance of NiFeS and NiFeCoS Nanosheet in Alkaline Seawater Medium at High Current Density

Building on the excellent performance of NiFeS and NiFeCoS nanosheet arrays in alkaline simulated seawater, their catalytic activity for OER was further evaluated in alkaline natural seawater (1.0 M KOH + seawater). As shown in **Figure** 4a,b, NiFeS and NiFeCoS exhibit remarkable OER activity in this environment, achieving a current density of 500 mA cm^{-2} at overpotentials of 332 and 349 mV, respectively. These values are significantly lower than those of NiFe LDH (365 mV) and NiFeCo LDH (410 mV). The corrosion resistance of these catalysts in alkaline seawater was also investigated. The corrosion potential follows the order as shown in Figure 4c and Table S7 (Supporting Information): NiFeCoS (0.341 V vs Hg/HgO) > NiFeS (−0.327 V vs Hg/HgO). Co-doping significantly enhances its corrosion resistance, demonstrating superior robustness for seawater electrolysis. Chronopotentiometry measurements further highlight the

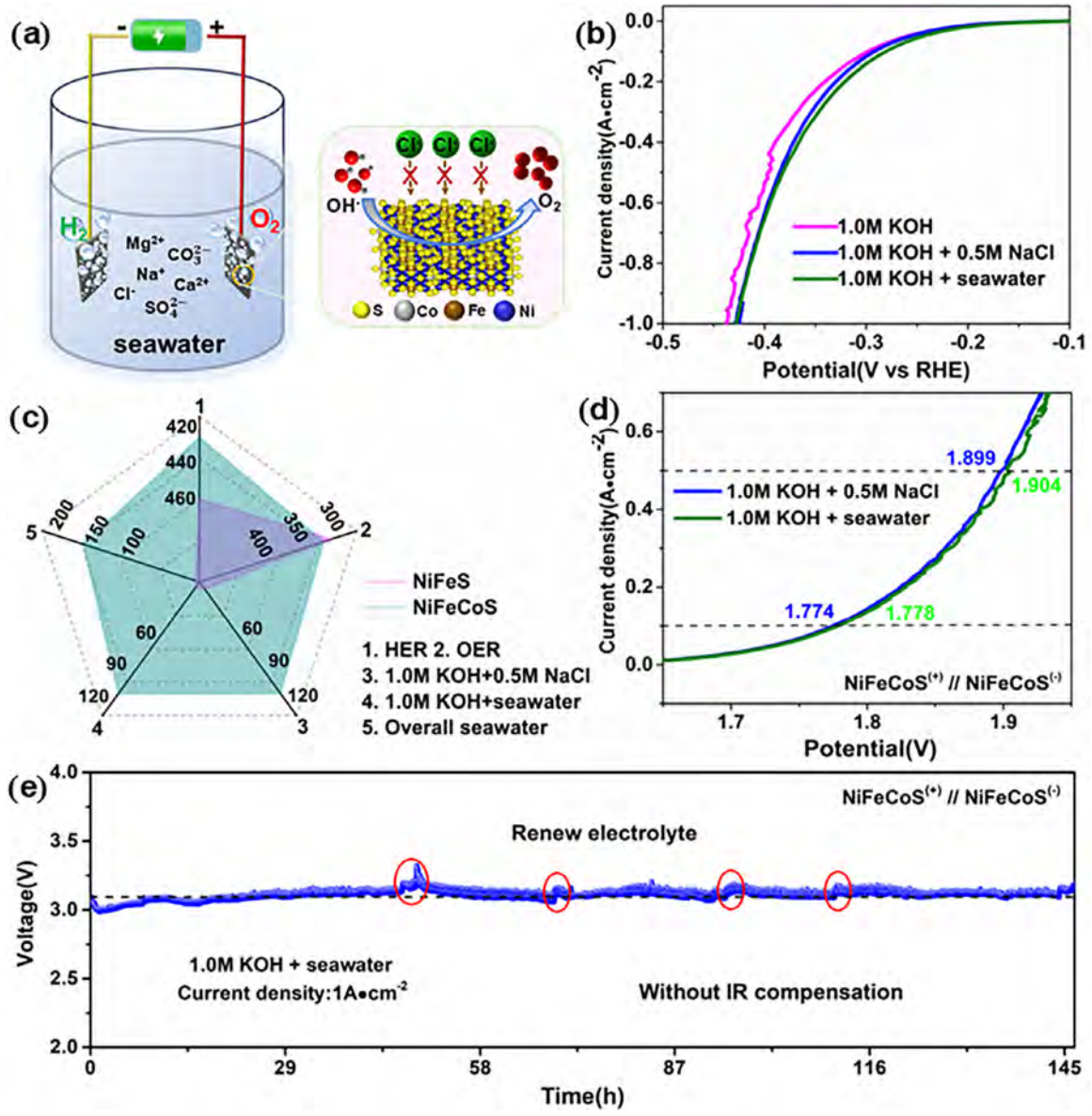

Figure 5. Overall water splitting. a) Schematic representation of the overall water splitting process, b) LSV curves of NiFeCoS electrode for the HER. c) Comparisons of NiFeS and NiFeCoS electrodes regarding OER and HER performance. d) Polarization curves of NiFeCoS || NiFeCoS in 1 M KOH + seawater. e) Chronopotentiometry curve of NiFeCoS || NiFeCoS under the corresponding potential at 1 A cm^{-2} for 148 h in alkaline natural seawater.

outstanding electrochemical stability of NiFeCoS nanosheets at 0.5 A cm^{-2} (Figure 4d). After 100 h of electrolysis, NiFeCoS shows a slight change in overpotential, whereas NiFeS exhibits significant decay within 10 h of operation (Figure 4d). The LSV curve for NiFeCoS measured after the durability test (Figure 4e) showed a notable increase in overpotential. The surface condition of the poststability test electrocatalyst was examined using SEM-EDS, revealing signals of Ca and Mg (Figure S12b, Supporting Information). Calcium and magnesium are commonly found in seawater, and the deposition of the related hydroxide, which covers the active sites on the surface, is one of the reasons for the performance degradation. The electrochemical performance of NiFeCoS was compared with previously reported materials (Tables S8–S11, Supporting Information), showing its superior performance and stability. Furthermore, the reaction selectivity was assessed by monitoring the concentration of ClO^- ions, which may form due to competitive ClER during seawater electrolysis. Using a colorimetric method based on ISO 7393-2:2017, no characteristic absorption peak of the Würster dye was observed in the UV–Vis absorption spectra even after 100 h with 1 A cm^{-2} (Figure S14, Supporting Information), confirming the excellent selectivity of NiFeCoS during the OER process in natural seawater without ClO^- formation.

The overall seawater-splitting performance of NiFeCoS in alkaline seawater was further evaluated (**Figure 5a**). Initially, the HER performance of NiFeCoS was investigated. NiFeCoS presents HER overpotentials of 300, 292, and 280 mV at a current density of 100 mA cm^{-2} in alkaline water, alkaline saline water,

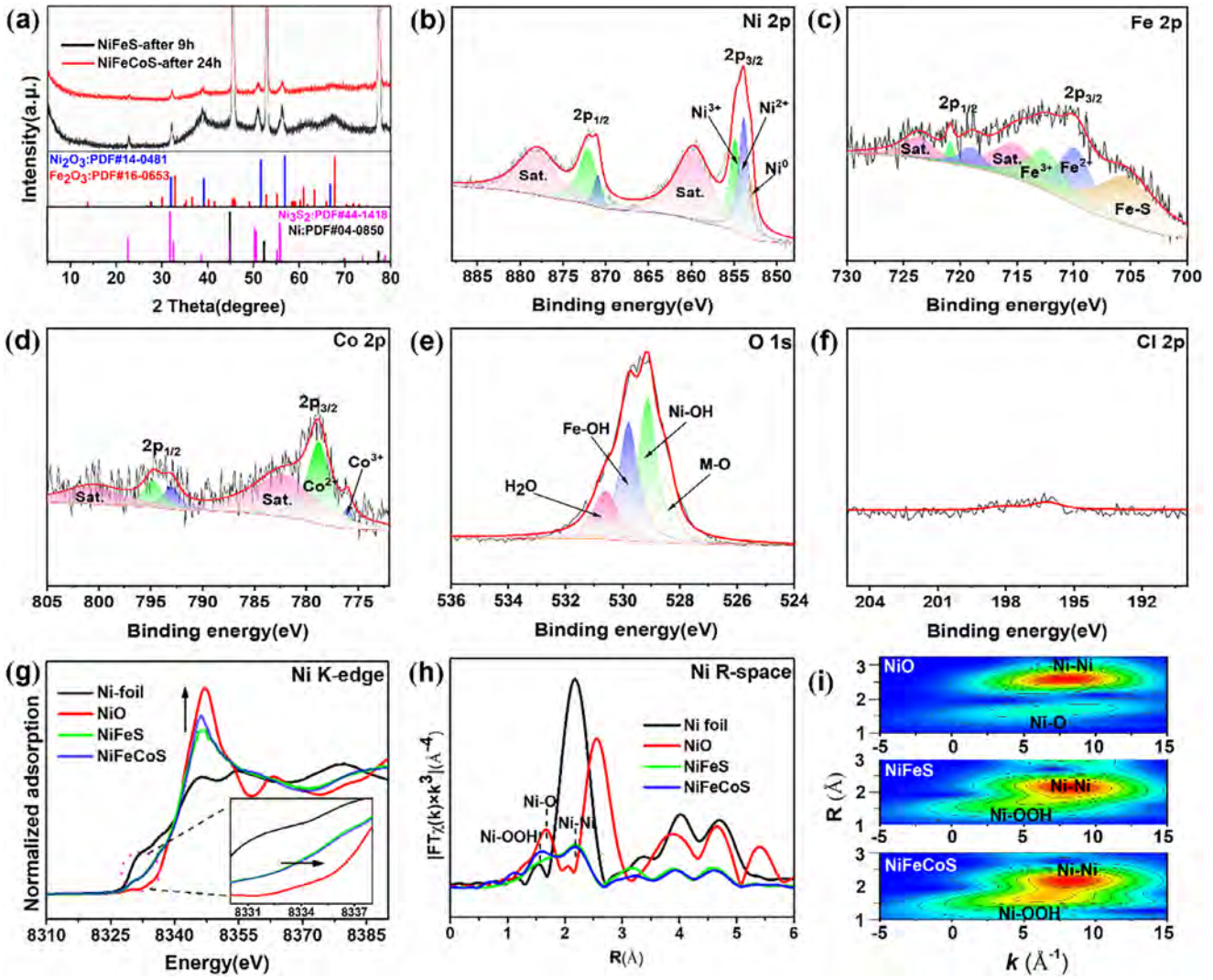

Figure 6. Crystal structure and surface chemical states characterization after stability test. a) XRD patterns of NiFeS and NiFeCoS after operation at 1 A cm^{-2}. XPS spectra b) Ni, c) Fe, d) Co, e) O, and f) Cl of NiFeCoS after 20 h of operation at 1 A cm^{-2} in the alkaline saline electrolyte, g) normalized XANES Ni K–edge spectra, h) Fourier-transform Ni K–edge EXAFS spectra, and i) wavelet transform contour plots of Ni of NiFeS and NiFeCoS after 20 h of operation at 0.5 A cm^{-2} in the alkaline saline electrolyte.

and alkaline natural seawater, respectively. Figure 5c comprehensively compares the HER, OER performance, and stability of NiFeS and NiFeCoS in different electrolytes. Based on its excellent HER and OER performance in alkaline seawater, a two-electrode configuration employing NiFeCoS as both cathode and anode was assembled for performance investigation. The LSV curves for $NiFeCoS^{(-)}//NiFeCoS^{(+)}$ in alkaline saline water and alkaline natural seawater are shown in Figure 5d. To achieve current densities of 100 and 500 mA cm^{-2} in alkaline saline water, the $NiFeCoS^{(-)}//NiFeCoS^{(+)}$ catalytic cell required cell voltages of 1.774 and 1.899 V, respectively, demonstrating excellent bifunctional activity. Similarly, in alkaline seawater, the cell required slightly higher cell voltages of 1.778 and 1.904 V to achieve the current densities of 100 and 500 mA cm^{-2}, highlighting the outstanding seawater-splitting activity of NiFeCoS. The stability of NiFeCoS for overall alkaline seawater splitting was examined under a high current density of 1 A cm^{-2} (Figure 5e). Remarkably, the electrocatalytic cell maintained a stable performance for 148 h, showcasing its long-term durability. Furthermore, gas analysis of the collected gases generated from the anode and cathode confirmed that only O_2 and H_2 were detected (Figure S16, Supporting Information), with no other undesirable gaseous by-products observed under the applied conditions. The experimental results highlight the potential of NiFeCoS nanosheets as industrial electrocatalysts for efficient and stable freshwater and seawater splitting, particularly at high current densities.

To investigate the activity and stability origin of NiFeCoS, XRD and XPS analyses were performed to examine the NiFeS and NiFeCoS after OER stability tests at 1 A cm^{-2}. XRD patterns (**Figure 6a**) revealed that both catalysts underwent a phase transformation from metal sulfides into metal oxides/hydroxides.[41] NiFeS showed a stronger Ni and Fe oxide peak after 9 h of operation, indicating a higher degree of oxidation. In contrast, the Ni and Fe oxide peak for NiFeCoS was significantly weaker,

demonstrating that the incorporation of Co species effectively mitigates material oxidation during electrolysis. XPS analysis further confirmed these findings by characterizing surface chemical compositions and valence states. The high-resolution Ni 2p spectrum (Figure 6b) of NiFeCoS displayed peaks at 854.0 and 872.1 eV for Ni $2p_{3/2}$ and Ni $2p_{1/2}$,[27] while Fe 2p peaks at 721.0 and 710.2 eV corresponded to Fe $2p_{1/2}$ and Fe $2p_{3/2}$.[29] The Co 2p spectrum (Figure 6c) of NiFeCoS showed peaks at 778.1 and 794.6 eV for Co $2p_{1/2}$ and Co $2p_{3/2}$.[33] In the O 1s spectrum (Figure 6e), the peaks can be attributed to M—OH and M—O groups, indicating the formation of metal hydroxide species (NiFeCoOOH).[42] Notably, the Cl 2p spectrum (Figure 6f) showed no chlorine signal after the stability test, highlighting the excellent ion selectivity of NiFeCoS during OER in alkaline saline water. Additionally, the S 2p spectrum indicated the presence of a small sulfur peak on the surface of NiFeCoS even after 20 h at 1 A cm^{-2} (Figure S17, Supporting Information). Whereas no sulfur peak was observed in NiFeS after 12 h at 300 mA cm^{-2} (Figures S18 and S19, Supporting Information), confirming that Co doping significantly slows metal sulfide oxidation. X-ray absorption spectroscopy (XAS) was conducted to further elucidate the electronic structure evolution induced by Co doping after the stability test. As shown in Figure 6g, the Ni K-edge X-ray absorption near-edge structure (XANES) spectra of post-stability-test NiFeS and NiFeCoS reveal distinct differences. Compared with NiFeS, the absorption edge of NiFeCoS exhibits a slight blue shift toward higher energy, indicating that the Ni species in NiFeCoS attain a higher valence state after the OER stability test due to Co incorporation.[34,43] Meanwhile, the enhanced white-line peak intensity in NiFeCoS suggests a decrease in the occupancy of Ni 3d orbitals, which can be attributed to electron transfer from Ni to Co.[35] Furthermore, the Fourier-transformed EXAFS spectra (Figure 6h) and the corresponding wavelet transform (WT) plots of Ni (Figure 6i) provide additional evidence that Co doping alters the local coordination environment around the Ni.[36,44] The advantages of doping processes mainly lie in their ability to significantly improve the electrical, magnetic, and optical properties of materials, which have been widely studied and are one of the primary methods for modifying high-performance materials.[29] In the reported study, theoretical calculations verified that the doping of V, Co, and Ir in the NiS_2 system significantly enhances the binding strength of sulfur atoms on the catalyst surface. The theoretical electric potential of the sulfide oxidation reaction (U_{SOR}) and the difference between the theoretical electric potential of the sulfide oxidation reaction(ΔU) represented the initiation electric potential of reconstruction and the intrinsic reconstruction abilities of metal sulfides. With the doping of V, Co, and Ir of pyrite-type NiS_2, the U_{SOR} shows a larger potential, and the ΔU shows a bigger value during OER.[45] Therefore, doping can enhance the resistance to reconstruction of material and stabilize the phases after reconstruction, while simple composites, due to weaker interatomic forces, exhibit a pronounced tendency toward structural reconstruction. Sun et al.[29] experimentally demonstrated that doping with cobalt can regulate the electronic structure of nickel sulfide. Co-doped Ni_3S_2 exhibits excellent corrosion resistance. After operating at high current density for 50 h, it still demonstrates outstanding catalytic performance. In our experiments, we found that NiFeCoS exhibits excellent dynamic and thermodynamic stability (Figure 6a), indicating that Co doping plays a critical role in slowing down metal sulfide oxidation and stabilizing the highly active Ni(Fe)OOH structure in the OER reaction kinetics.[29]

3. Theoretical Calculation

For the sake of further exploring the mechanism of enhanced resistance to Cl^- corrosion by Co species, density functional theory (DFT) calculations were carried out. The structural models of NiFeS and NiFeCoS are depicted in Figure S20 (Supporting Information). **Figure** 7a,b presents the charge distribution of NiFeS and NiFeCoS with Cl^- adsorption. NiFeS exhibits a stronger electronic interaction with Cl^-, showing a more pronounced electron cloud. In contrast, introducing Co into the NiFeS system results in a diminished electron cloud in NiFeCoS, suggesting weaker Cl^- adsorption. Figure 7c further reveals that Ni and Fe sites become more stable after introducing Co, indicating that Co effectively stabilizes the NiFeS system, consistent with the experimental results. Additionally, Figure 7d shows the calculated Cl^- and OH^- adsorption energies to support this conclusion. The Cl^- adsorption energy on NiFeS is −2.523 eV, while it is increased to −2.178 eV on NiFeCoS. In contrast, OH^- adsorption strengthens, decreasing the energy from −2.923 eV on NiFeS to −3.862 eV on NiFeCoS. NiFeCoS shows a more positive Cl^- adsorption energy, suggesting that the doping of Co could effectively weaken the adsorption of Cl^- on the surface of the material and improve the ion selectivity in the OER, which is beneficial for the OER and for resisting chloride-induced corrosion. Total density of states (TDOS) analysis (black curve) shows that NiFeS and NiFeCoS exhibit metallic character, with substantial electronic states near the Fermi level, as shown in Figure 7e,f. From the projected density of states (PDOS), the Ni-d orbitals are identified as the primary contributors to electronic conduction, particularly in the range of −3 to +1 eV, near the Fermi level. Fe-d orbitals also contribute significantly within the same energy range, though to a slightly lesser extent. After Co-doping, the Co-d orbitals participate in conduction as well, complementing the electronic structure of NiFeS. In contrast, the S-p orbitals are mostly distributed from −6 to −3 eV and contribute predominantly to the valence band, with minimal contribution near the Fermi level. Overall, the introduction of Co not only enhances the structural stability of the NiFeS catalyst but also improves ion selectivity by weakening Cl^- adsorption, thus mitigating Cl^--induced corrosion and enhancing the long-term durability of the material in Cl^--containing electrolytes.

4. Conclusion

In summary, the NiFeCoS electrode was successfully synthesized on NF using a straightforward room-temperature technique followed by a solvothermal sulfurization process. Both experimental and theoretical analyses demonstrate that the Fe and Co co-doped Ni_3S_2 exhibits remarkable bifunctional electrocatalytic activity and exceptional stability under high current densities in both alkaline media and seawater environments, achieving overpotentials of 261 and 270 mV, respectively, to sustain a current density of 100 mA cm^{-2}. Moreover, the NiFeCoS electrode showcases impressive performance at elevated current densities, maintaining

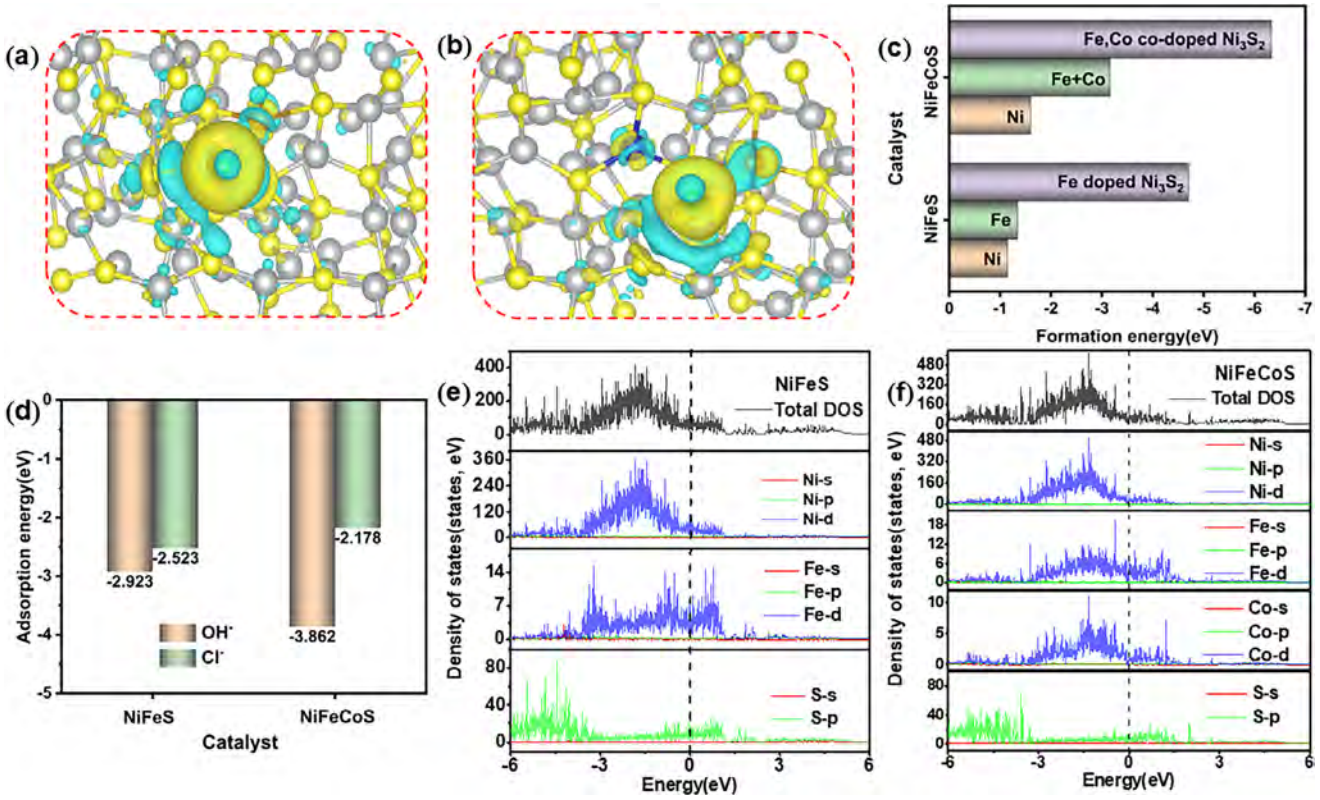

Figure 7. DFT calculations. a,b) The charge density difference of NiFeS and NiFeCoS. Note that the gray, brown, blue, yellow, and green spheres correspond to Ni, Fe, Co, S, and Cl atoms. c) formation energy of NiFeS and NiFeCoS, d) adsorption energies with Cl^- and OH^-. e,f) TDOS and PDOS of NiFeS and NiFeCoS, the s, p, and d orbitals represented by red, green, and blue.

stability for 148 h. Incorporating cobalt optimizes the electronic configuration of nickel, iron, and sulfur elements, effectively decelerating the oxidation rate and enhancing the stability of metal hydroxides during the oxygen evolution reaction in seawater. This study introduces a novel approach for the design and synthesis of advanced multiphase nanocomposites, paving the way for their application in seawater electrolysis.

Supporting Information

Supporting Information is available from the Wiley Online Library or from the author.

Acknowledgements

The "Network Joint Research Center for Materials and Devices" supported this work by the Ministry of Education, Culture, Sports, Science and Technology (MEXT). The first author is supported by the China Scholarship Council (No. 202308620078). The authors would like to express their sincere gratitude for the support provided by Su Pan and Mizuki Takahashi from Professor Hayashi's research laboratory.

Conflict of Interest

The authors declare no conflict of interest.

Author Contributions

Y.S. performed methodology, validation, formal analysis, and wrote the original draft. Y.S. performed testing support. Y.Z. performed a theoretical calculation. T.Y., J.C.H., and S.Y. performed conceptualization, reviewed, and edited.

Data Availability Statement

The data supporting this study's findings are available from the corresponding author upon reasonable request.

Keywords

Iron and cobalt co-doped nickel sulfides, non-noble metal electrocatalysts, oxygen evolution reaction (OER), seawater electrolysis

Received: July 13, 2025
Revised: October 9, 2025
Published online:

[1] A. Li, S. Kong, C. Guo, H. Ooka, K. Adachi, D. Hashizume, Q. Jiang, H. Han, J. Xiao, R. Nakamura, *Nat. Catal.* **2022**, *5*, 109.
[2] P. C. Yu, X. L. Zhang, T. Y. Zhang, X. Y. Tao, Y. Yang, Y. H. Wang, S. C. Zhang, F. Y. Gao, Z. Z. Niu, M. H. Fan, M. R. Gao, *J. Am. Chem. Soc.* **2024**, *146*, 20379.

[3] J. Zhang, Q. Zhang, X. Feng, *Adv. Mater.* **2019**, *31*, 1808167.
[4] S. Jiang, R. Zhang, H. Liu, Y. Rao, Y. Yu, S. Chen, Q. Yue, Y. Zhang, Y. Kang, *J. Am. Chem. Soc.* **2020**, *142*, 6461.
[5] L. Huang, D. Chen, G. Luo, Y. R. Lu, C. Chen, Y. Zou, C. L. Dong, Y. Li, S. Wang, *Adv. Mater.* **2019**, *31*, 1901439.
[6] S. Ding, Z. Li, G. Lin, L. Wang, A. Dong, L. Sun, *ACS Energy Lett.* **2024**, *9*, 3719.
[7] C. F. Du, K. N. Dinh, Q. Liang, Y. Zheng, Y. Luo, J. Zhang, Q. Yan, *Adv. Energy Mater.* **2018**, *8*, 1801127.
[8] Z. Li, M. Hu, P. Wang, J. Liu, J. Yao, C. Li, *Coord. Chem. Rev.* **2021**, *439*, 213953.
[9] Z. Li, Y. Yao, S. Sun, J. Liang, S. Hong, H. Zhang, C. Yang, X. Zhang, Z. Cai, J. Li, Y. Ren, Y. Luo, D. Zheng, X. He, Q. Liu, Y. Wang, F. Gong, X. Sun, B. Tang, *Angew. Chem. Int. Ed. Engl.* **2024**, *63*, 202316522.
[10] H. Liu, W. Shen, H. Jin, J. Xu, P. Xi, J. Dong, Y. Zheng, S. Z. Qiao, *Angew. Chem. Int. Ed. Engl.* **2023**, *62*, 202311674.
[11] J. Sun, P. Song, H. Zhou, L. Lang, X. Shen, Y. Liu, X. Cheng, X. Fu, G. Zhu, *Appl. Surf. Sci.* **2021**, *567*, 150757.
[12] M. Yu, J. Li, F. Liu, J. Liu, W. Xu, H. Hu, X. Chen, W. Wang, F. Cheng, *J. Energy Chem.* **2022**, *72*, 361.
[13] L. Yu, Q. Zhu, S. Song, B. McElhenny, D. Wang, C. Wu, Z. Qin, J. Bao, Y. Yu, S. Chen, Z. Ren, *Nat. Commun.* **2019**, *10*, 5106.
[14] Z. Cai, J. Liang, Z. Li, T. Yan, C. Yang, S. Sun, M. Yue, X. Liu, T. Xie, Y. Wang, T. Li, Y. Luo, D. Zheng, Q. Liu, J. Zhao, X. Sun, B. Tang, *Nat. Commun.* **2024**, *15*, 6624.
[15] H. Chen, R. T. Gao, H. Chen, Y. Yang, L. Wu, L. Wang, *Adv. Funct. Mater.* **2024**, *34*, 2315674.
[16] H.-M. Zhang, L. Zuo, Y. Gao, J. Guo, C. Zhu, J. Xu, J. Sun, *J. Mater. Sci. Technol.* **2024**, *173*, 1.
[17] M. Li, H.-J. Niu, Y. Li, J. Liu, X. Yang, Y. Lv, K. Chen, W. Zhou, *Appl. Catal., B* **2023**, *330*, 122612.
[18] P. Li, S. Zhao, Y. Huang, Q. Huang, B. Xi, X. An, S. Xiong, *Adv. Energy Mater.* **2023**, *14*, 2303360.
[19] F.-Y. Gao, P.-C. Yu, M.-R. Gao, *Curr. Opin. Chem. Eng.* **2022**, *36*, 100827.
[20] S. Dresp, F. Dionigi, M. Klingenhof, P. Strasser, *ACS Energy Lett.* **2019**, *4*, 933.
[21] C. Huang, Q. Zhou, D. Duan, L. Yu, W. Zhang, Z. Wang, J. Liu, B. Peng, P. An, J. Zhang, L. Li, J. Yu, Y. Yu, *Energy Environ. Sci.* **2022**, *15*, 4647.
[22] G. Bahuguna, B. Filanovsky, F. Patolsky, *Nano Energy* **2023**, *111*, 108439.
[23] J. Chen, L. Zhang, J. Li, X. He, Y. Zheng, S. Sun, X. Fang, D. Zheng, Y. Luo, Y. Wang, J. Zhang, L. Xie, Z. Cai, Y. Sun, A. A. Alshehri, Q. Kong, C. Tang, X. Sun, *J. Mater. Chem. A* **2023**, *11*, 1116.
[24] L. E. Mofokeng, E. Makhado, P. Ndungu, *J. Ind. Eng. Chem.* **2024**, *144*, 48.
[25] G. Wang, T. Xiang, X. Ren, L. Zhang, C. Chen, *Int. J. Hydrogen Energy* **2024**, *73*, 775.
[26] X. Zhao, X. Shang, Y. Quan, B. Dong, G.-Q. Han, X. Li, Y.-R. Liu, Q. Chen, Y.-M. Chai, C.-G. Liu, *Electrochim. Acta* **2017**, *230*, 151.
[27] L. Zhao, M. Wen, Y. Guo, Q. Wu, Q. Zhu, Y. Fu, *Adv. Funct. Mater.* **2023**, *33*, 2308422.
[28] Z. Zeb, Y. Huang, L. Chen, R. Gao, X. Gao, M. Sun, H. Cai, J. Chen, F. Abbas, M. Liao, L. Ni, Y. Wei, *J. Colloid Interface Sci.* **2025**, *686*, 289.
[29] M. Yue, X. He, S. Sun, Y. Sun, M. S. Hamdy, M. Benaissa, A. A. M. Salih, J. Liu, X. Sun, *Nano Res.* **2023**, *17*, 1050.
[30] Z. Yousefi, A. A. Asgharinezhad, A. Larimi, C. Ghotbi, *J. Alloys Compd.* **2024**, *1002*, 175214.
[31] C. Shi, J. Zhou, M. A. Boda, K. Zhao, Z. Yang, D. Yuan, Z. Yi, *J. Mater. Chem. A* **2025**, *13*, 4538.
[32] R. Iwata, L. Zhang, K. L. Wilke, S. Gong, M. He, B. M. Gallant, E. N. Wang, *Joule* **2021**, *5*, 887.
[33] C. Feng, M. Chen, Y. Zhou, Z. Xie, X. Li, P. Xiaokaiti, Y. Kansha, A. Abudula, G. Guan, *J. Colloid Interface Sci.* **2023**, *645*, 724.
[34] W. Xu, R. Zhao, Q. Li, B. Sun, J. Wu, W. Zhong, Y. Gao, X. Nan, Q. Huang, Y. Yang, X. Li, N. Yang, Q. Zhang, *Adv. Energy Mater.* **2023**, *13*, 2300978.
[35] Y. Wang, S. Tao, H. Lin, G. Wang, K. Zhao, R. Cai, K. Tao, C. Zhang, M. Sun, J. Hu, B. Huang, S. Yang, *Nano Energy* **2021**, *81*, 105606.
[36] L. Shao, X. Han, L. Shi, T. Wang, Y. Zhang, Z. Jiang, Z. Yin, X. Zheng, J. Li, X. Han, Y. Deng, *Adv. Energy Mater.* **2023**, *14*, 2303261.
[37] J. Liu, T. Wang, M. Sun, M. Liao, S. Wang, S. Liu, H. Shi, Y. Liu, Y. Shen, R. Cao, Y. Huang, B. Huang, Q. Li, *J. Am. Chem. Soc.* **2024**, *146*, 33276.
[38] A. Naderi, X. Yong, M. Karamad, J. Cai, Y. Zang, I. Gates, S. Siahrostami, G. Wang, *Appl. Surf. Sci.* **2021**, *542*, 148681.
[39] F. N. I. Sari, Y. C. Lai, Y. J. Huang, X. Y. Wei, H. Pourzolfaghar, Y. H. Chang, M. Ghufron, Y. Y. Li, Y. H. Su, O. Clemens, J. M. Ting, *Adv. Funct. Mater.* **2024**, *34*, 2310181.
[40] X. Wang, X. Xu, Y. Nie, R. Wang, J. Zou, *Adv. Sci. (Weinh)* **2023**, *10*, 2301961.
[41] G. Wu, M. Chen, X. Du, X. Zhang, *Fuel* **2024**, *368*, 131660.
[42] Y. Zhuo, D. Liu, L. Qiao, S. Chen, J. Lu, W. F. Ip, H. Pan, Z. Wang, *Adv. Energy Mater.* **2023**, *13*, 2301912.
[43] G. Mu, G. Wang, Q. Huang, Y. Miao, D. Wen, D. Lin, C. Xu, Y. Wan, F. Xie, W. Guo, R. Zou, *Adv. Funct. Mater.* **2023**, *33*, 211260.
[44] Z. X. Qian, G. H. Liang, L. F. Shen, G. Zhang, S. Zheng, J. H. Tian, J. F. Li, H. Zhang, *J. Am. Chem. Soc.* **2025**, *147*, 1334.
[45] W. Wang, A. Wang, J. Xu, H. Li, M. Yu, A. Dong, Z. Li, C. Zhao, F. Cheng, W. Wang, *J. Colloid Interface Sci.* **2024**, *657*, 334.